



Analysis of droplet evaporation in isotropic turbulence through droplet-resolved DNS

Michael S. Dodd^{a,b,*}, Danyal Mohaddes^c, Antonino Ferrante^d, Matthias Ihme^{a,c}

^a Center for Turbulence Research, Stanford University, Stanford, CA 94305, United States

^b Independent Scholar, Bellevue, WA 98005

^c Department of Mechanical Engineering, Stanford University, Stanford, CA 94305, United States

^d Department of Aeronautics & Astronautics, University of Washington, Seattle, WA 98195, United States

ARTICLE INFO

Article history:

Received 11 August 2020

Revised 14 February 2021

Accepted 24 February 2021

Keywords:

Droplets

Turbulence

Evaporation

Spray combustion

Direct numerical simulation

ABSTRACT

Direct numerical simulations (DNS) of the evaporation of interface-resolved *n*-heptane fuel droplets in forced homogeneous isotropic turbulence (HIT) are performed at 10 bar and 348 K. A parametric study is conducted in which the ratio of initial droplet diameter to Kolmogorov lengthscale and the liquid volume fraction are varied in the ranges $0 < d_0/\eta \leq 17$ and $10^{-4} \leq \alpha_l \leq 10^{-2}$, respectively. The DNS results are validated against experimental data for an isolated droplet evaporating in HIT. Our results show that increasing the liquid volume fraction of droplets decreases the evaporation rate and causes the evaporation rate to deviate from the classical d^2 -law. Evaporation models based on the Frössling correlation are tested in an *a priori* study using the DNS results. It is shown that, in general, the Frössling correlation is inaccurate when predicting the droplet Sherwood number in turbulent conditions. Modeling aspects of the Spalding number in the context of multiple interacting droplets are discussed.

© 2021 Elsevier Ltd. All rights reserved.

1. Introduction

The evaporation of liquid droplets in turbulent environments is a key phenomenon in spray combustion and hence of relevance to gas turbines, internal combustion engines and rocket propulsion [1–3]. In these systems, the coupling of droplet evaporation and turbulence is inherent to the design and directly impacts fuel consumption, performance and emissions. As such, the reliable prediction of evaporation in these systems is critical to their numerical modeling and therefore improvements in their design.

The interaction of liquid fuel droplets with turbulence occurs across a broad range of scales in practical systems. Considering a turbulent flow with an integral time scale τ_0 , Kolmogorov time scale τ_η and droplet relaxation time $\tau_d = (\rho_l d_0^2)/(18\mu_g)$, where ρ_l is the liquid density, d_0 the droplet diameter and μ_g the dynamic gas viscosity, two characteristic non-dimensional groups may be formed, namely the integral-scale and Kolmogorov-scale Stokes numbers $St = \tau_d/\tau_0$ and $St_\eta = \tau_d/\tau_\eta$, respectively [4]. Applying the relevant time scale definitions and assuming a fully developed turbulence cascade yields the scaling relation $St_\eta \sim St Re^{1/2}$, where Re is the Reynolds number based on the integral length scale,

from which it can be shown that $d_0/\eta \sim (St_\eta(\rho_g/\rho_l))^{1/2}$. For typical engineering devices such as aviation gas-turbine combustors [5], $\rho_g/\rho_l \sim 10^{-2}$ and $10^0 \lesssim St_\eta \lesssim 10^4$, yielding $10^{-1} \lesssim d_0/\eta \lesssim 10^1$. In spray processes, the description of droplet interactions requires consideration of the liquid volume fraction α_l , which has been shown to be $\mathcal{O}(10^{-3})$ near the flame zone [6], and possibly higher near the injector.

Most simulations of spray evaporation and liquid fuel combustion employ point-particle methods in conjunction with finite-volume solvers [7]. In these methods, the liquid-phase governing equations are reduced to a set of Lagrangian equations and solved for each droplet individually. Then, they are coupled to the gas-phase Eulerian equations with evaporative fluxes modeled using empirically-corrected Spalding number formulations [8]. Point-particle methods assume scale separation between d_0 and η [9], and are hence only valid when $d_0/\eta < 1$ and $d_0/\Delta < 1$, where Δ is the grid spacing. Apart from Lagrangian formulations, Eulerian methods have also been examined to model spray combustion using population balance equations [10].

Direct numerical simulations (DNS) of evaporating droplets interacting with turbulence using the point-particle approach have been conducted in homogeneous shear flows [11] and temporally developing mixing layers [12]. There has also been extensive use of DNS/point-particles to study droplets in spray applications and reacting flows [13–19]. To improve these models, further understand-

* Corresponding author at: Center for Turbulence Research, Stanford University, Stanford, CA 94305, United States.

E-mail address: mchl.dodd@gmail.com (M.S. Dodd).

ing of the interaction between droplets and turbulence for conditions in which the droplet diameter becomes comparable or exceeds the characteristic scales of the turbulence is needed. The simultaneous increase in computational resources and development of high-fidelity numerical methods for gas-liquid flows has enabled such particle- and droplet-resolved simulations in turbulent flows [20]. In particular, advances in methods to model phase change [21–24] have allowed resolving flows around Kolmogorov-scale-size droplets or larger ($d_0/\eta \geq 1$), so-called “finite-size” droplets. Modulation of small-scale turbulence and the scalar mixing process by droplets can be fully resolved [25].

DNS of a stationary evaporating droplet in a uniform flow with steady and unsteady wakes has been conducted [24,26]. There have also been a limited number of detailed simulations in turbulent flows that resolve the heat and mass transfer processes from evaporating droplets, but many neglect physical processes such as interface recession and Stefan flow [27] or droplet deformation, flow inside the droplets, and temperature variations on the droplet surface [28]. In the present work, we perform DNS of finite-size deformable droplets in homogeneous isotropic turbulence (HIT) in which the exchange of mass, momentum, and heat between the turbulent gas phase and the liquid droplets is resolved. The objective of this study is to improve the fundamental understanding of the mechanisms of evaporating droplets and turbulence interaction. To this end, we consider a broad parameter space to cover a wide range of relevant operating conditions. Validation with recent experimental measurements of turbulent droplet evaporation [29] is included, and a priori studies of evaporation models are performed.

The remainder of the manuscript has the following structure. The governing equations and numerical methods for the DNS study are presented in Section 2. The experimental and numerical setup considered is described in Section 3. Results are presented in Section 4, and the manuscript closes with conclusions in Section 5.

2. Mathematical formulation

2.1. Governing equations

We consider a gas-liquid flow with phase change in the low-Mach-number limit. In this limit, the liquid phase is assumed incompressible and the gas phase is compressible, but acoustic effects are removed. The liquid phase (V_l) is described by a single-component hydrocarbon fuel, namely n -heptane, and the gas phase (V_g) consists of nitrogen as an inert gas and the evaporating heptane vapor. Throughout this paper, the subscripts l and g are used to denote liquid- and gas-phase quantities, respectively. The conservation equations for mass, momentum, energy, and vapor species in both phases are

$$D_t \rho = -\rho \nabla \cdot \mathbf{u}, \quad (1a)$$

$$\rho D_t \mathbf{u} = -\nabla p + \nabla \cdot \boldsymbol{\tau} + \mathbf{f}_\sigma + \mathbf{f}_m, \quad (1b)$$

$$\rho c_p D_t T = d_t p_0 + \nabla \cdot (\lambda \nabla T) - \Delta h_v \dot{m}'' \delta_\Sigma, \quad (1c)$$

$$\rho_g D_t Y_v = \nabla \cdot (\rho_g \mathcal{D} \nabla Y_v), \quad (1d)$$

where $D_t = \partial/\partial t + (\mathbf{u} \cdot \nabla)$, $d_t = d/dt$, ρ is the density, p is the hydrodynamic pressure, \mathbf{u} is the velocity, $\boldsymbol{\tau}$ is the viscous stress tensor, c_p is the specific heat capacity at constant pressure, T is the temperature, p_0 is the thermodynamic pressure, λ is the thermal conductivity, Δh_v is the enthalpy of vaporization, \mathcal{D} is the mass

diffusivity, and Y_v is the n -heptane vapor mass fraction. The nitrogen mass fraction is then $Y_{N_2} = 1 - Y_v$. The force term due to surface tension is

$$\mathbf{f}_\sigma = \sigma \kappa \delta_\Sigma \mathbf{n}, \quad (2)$$

where σ is the surface tension coefficient, κ is the interface curvature, \mathbf{n} is a unit normal vector directed into the liquid phase, and δ_Σ is the surface Dirac δ -function which is non-zero only at the interface Σ . The force due to phase change in Eq. (1b) takes the form

$$\mathbf{f}_m = (\dot{m}'')^2 \left(\frac{1}{\rho_g} - \frac{1}{\rho_l} \right) \delta_\Sigma \mathbf{n}, \quad (3)$$

where \dot{m}'' is the mass flux due to phase change

$$\dot{m}'' = \frac{\mathcal{D} \rho_g}{1 - Y_v} \nabla Y_v \cdot \mathbf{n}. \quad (4)$$

Note that $d_t p_0 = 0$ in the liquid phase due to incompressibility. We use the sign convention that $\dot{m}'' > 0$ for evaporation and $\dot{m}'' < 0$ for condensation. Because the liquid phase consists of a single-component fuel, Eq. (1d) is only solved in the gas phase. A Dirichlet boundary condition for Y_v is applied at the interface assuming mixture saturation conditions. The vapor pressure of the fuel at the interface is related to the temperature from the Antoine equation [30]. The fluid properties μ , c_p , and λ are computed as $\phi = (1 - H)\phi_g + H\phi_l$, where ϕ_g and ϕ_l are thermo-transport properties and $H = H(\mathbf{x}, t)$ is the Heaviside function evaluated at position \mathbf{x} and time t , which has value $H = 0$ in the gas phase and $H = 1$ in the liquid phase. The density of the liquid phase ρ_l is constant, while the density of the gas phase ρ_g can vary in space and in time through the ideal-gas equation of state. The quantities $\mu = \mu(T)$ and $c_p = c_p(T)$ are temperature dependent and computed using Sutherland's law [31] and NASA polynomials [32], respectively. The thermal conductivity $\lambda = \lambda(T)$ is computed by assuming constant Prandtl number ($Pr = c_p \mu / \lambda$), and the mass diffusivity $\mathcal{D} = \mathcal{D}(T)$ is computed by assuming constant but non-unity Lewis number ($Le = Sc/Pr = \lambda / (\rho c_p \mathcal{D})$). Because the temperature considered in the simulations is sufficiently far from the boiling point of n -heptane and $\alpha_l \leq 10^{-2}$, vapor mass fractions are expected to be low, and consequently variations in thermo-physical properties due to composition are neglected. At $Y_v = 0.06$, μ , λ , $c_{p, \text{mass}}$, \mathcal{D} have an error 4%, 1%, 5%, and < 1%, respectively, relative to their composition-dependent counterparts computed using Cantera [33,34].

Under the low-Mach and incompressible flow assumptions, the continuity equation (Eq. (1a)) can be rewritten in the form of a divergence constraint on the velocity field [35]

$$\nabla \cdot \mathbf{u} = \begin{cases} -\frac{1}{p_0} d_t p_0 + \frac{1}{T} D_t T + \left(\frac{\bar{\mathcal{M}}}{\mathcal{M}_l} - \frac{\bar{\mathcal{M}}}{\mathcal{M}_a} \right) D_t Y_v & \mathbf{x} \in V_g \\ \dot{m}'' (\rho_g^{-1} - \rho_l^{-1}) \delta_\Sigma & \mathbf{x} \in \Sigma, \\ 0 & \mathbf{x} \in V_l \end{cases} \quad (5)$$

where in the gas phase V_g there is expansion or contraction due to the low-Mach-number formulation, at the interface Σ there is expansion due to evaporation or compression by condensation, and in the liquid phase V_l the velocity field is divergence-free due to incompressibility conditions. In Eq. (5), \mathcal{M}_l is the molar mass of the liquid-phase (n -heptane), \mathcal{M}_a is the molar mass of the ambient gas (nitrogen) and $\bar{\mathcal{M}}$ is the mass-averaged molar mass of the mixture. Eq. (5), as opposed to Eq. (1a), is used to enforce mass conservation.

To close the set of equations, we use the fact that the domain is isochoric with periodic boundary conditions to determine the change in thermodynamic pressure:

$$d_t p_0 = \frac{p_0}{V_g} \left\{ \int_V \dot{m}'' \left(\frac{1}{\rho_g} - \frac{1}{\rho_l} \right) \delta_\Sigma dV + \int_{V_g} \left[\frac{1}{T} D_t T + \left(\frac{\bar{M}}{\mathcal{M}_l} - \frac{\bar{M}}{\mathcal{M}_a} \right) D_t Y_v \right] dV \right\}, \quad (6)$$

where $V = V_l \cup V_g$.

2.2. Numerical method

The governing equations are discretized on a uniform staggered Cartesian mesh using second-order central differences with the velocity components located at cell faces and all other quantities cell-centered. The equations are discretized in time using the second-order Adams-Bashforth scheme. Mass conservation is satisfied to machine accuracy by enforcing the divergence constraint on the velocity field (Eq. (5)) using the FastP* method [36]. The Poisson equation for pressure is solved using an FFT-based solver.

The phase indicator function H is discretized using the volume-of-fluid method. We use a mass-conserving volume-of-fluid method [37] to transport the volume fraction field C , which is defined as the volume fraction of liquid in each computational cell. It has the property $C = 1$ in the liquid phase, $C = 0$ in the gas phase, and $0 < C < 1$ in computational cells containing the interface. The surface Dirac δ -function, δ_Σ , is discretized using the continuum surface force approach [38]. The full numerical methodology for simulating gas-liquid flows with phase change has been verified and validated [35].

3. Numerical and computational setup

We consider three-dimensional HIT in a cubic domain with periodic boundary conditions in three spatial directions. The gas phase is initially nitrogen and the liquid phase is n -heptane. The diffusion of nitrogen into the liquid phase is neglected. The initial temperature and pressure of the system are uniform at 348 K and 10 bar, respectively, and were chosen for relevance to gas turbine combustion applications [39,40]. Two key non-dimensional parameters are varied, namely the ratio of initial droplet diameter to Kolmogorov lengthscale d_0/η and the liquid volume fraction $\alpha_l = V_l/V$. The flow properties and computational parameters are summarized in Table 1. The chosen conditions are relevant to aeronautical spray combustion devices. We note that in the present study, since the gaseous Schmidt number $Sc_g = \mu_g/(\rho_g D) = 2.81 > 1$, the Batchelor scale λ_B describing the dissipation of scalar fields is finer than η as $\lambda_B/\eta = Sc_g^{-1/2} \approx 0.6$. Since the liquid fuel is monocomponent and the ambient gas is taken to be insoluble in the liquid phase, the liquid phase turbulence is not relevant to scalar mixing.

A grid convergence study was performed which confirmed that a resolution of 14 grid points per droplet diameter was sufficient for resolving the scalar and momentum turbulence length scales and the transition region at the liquid-gas interface.

Cases 1–3 are designed to mimic experiments that were conducted in a pressurized turbulence chamber driven by four pairs of axially opposed fans [29], creating statistically stationary forced HIT in the center of the apparatus. Experiments were conducted using a range of droplet diameters and fan speeds, resulting in a range of d_0/η for which the rate of droplet evaporation was measured. In each experiment, a single droplet was suspended and held fixed by two crossed microfibers. To this end, a proportional controller is employed for simulations of Cases 1–3 to keep the center of mass of the n -heptane droplet in its initial position. Varying d_0/η is conducted on a 224^3 computational mesh for a single droplet with initial diameter $d_0 = 200 \mu\text{m}$.

Cases 4–6 consider effects of increasing α_l , which in turn decreases the inter-droplet spacing. These simulations are performed

Table 1

Physical and computational parameters: initial droplet diameter d_0 , side length of the computational domain L , turbulence r.m.s. velocity U_{rms} , Kolmogorov time scale τ_η , turbulent droplet Stokes number $St_\eta = \tau_d/\tau_\eta$, integral-scale Reynolds number $Re = k^2/(\epsilon \nu)$, Taylor-microscale Reynolds number $Re_\lambda = U_{rms} \lambda/\nu$, initial droplet Weber number $We_{rms} = \rho_g U_{rms}^2 d_0/\sigma$, gas-phase Prandtl number $Pr_g = c_{p,g} \mu_g/\lambda_g$, liquid-phase Prandtl number $Pr_l = c_{p,l} \mu_l/\lambda_l$, gas-phase Schmidt number $Sc_g = \mu_g/(\rho_g D)$, gas-phase Lewis number $Le_g = Sc_g/Pr_g$, initial liquid volume fraction α_l , and initial number of droplets N_d .

Case	1	2	3	4	5	6
d_0 [μm]	200	200	200	40	40	40
L [mm]	3.2	3.2	3.2	2.56	2.56	2.56
U_{rms} [m/s]	0	0.22	0.43	0.68	0.68	0.68
τ_η [μs]	–	14.0	11.8	10.0	10.0	10.0
d_0/η	0	14.3	17.0	4.0	4.0	4.0
St_η	0	748	1060	59.5	59.5	59.5
Re	0	141	282	358	358	358
Re_λ	0	30.7	43.3	48.8	48.8	48.8
$We_{rms} (\times 10^{-3})$	0	4.43	17.7	8.91	8.91	8.91
Pr_g	0.715	0.715	0.715	0.715	0.715	0.715
Pr_l	5.51	5.51	5.51	5.51	5.51	5.51
Sc_g	2.81	2.81	2.81	2.81	2.81	2.81
Le_g	3.93	3.93	3.93	3.93	3.93	3.93
$\alpha_l (\times 10^{-4})$	1.28	1.28	1.28	1	10	100
N_d	1	1	1	51	501	5007

on a 896^3 mesh. The droplets are initially spherical with a diameter of $d_0 = 40 \mu\text{m}$ and randomly and homogeneously seeded throughout the computational domain. The volume fraction α_l is increased by increasing the number of droplets N_d . Unlike Cases 1–3, the droplets for Cases 4–6 move freely in order to model realistic conditions inside a combustor.

Case 1 considers a single droplet in a quiescent environment. For Cases 2–6, the turbulent kinetic energy (TKE) of the gas phase is kept constant by using a standard band-limited forcing scheme in which the kinetic energy is only injected into the first two wavenumber shells ($1 \leq \kappa/\kappa_{min} \leq 2$), where κ_{min} is the lowest non-zero wavenumber $\kappa_{min} = 2\pi/L$, and L is the length of the computational domain. The initial velocity field was generated by prescribing the turbulence kinetic energy spectrum as $E(\kappa) \propto (\kappa/\kappa_{peak}^2) \exp(-\kappa/\kappa_{peak})$, where the wavenumber with peak energy is $\kappa_{peak} = 1$. We ensure that the initial random velocity field is isotropic and divergence-free with respect to the discretized form of the continuity equation and that the velocity cross-correlation spectra, $R_{ij}(\kappa)$, satisfy the realizability constraint [41]. In the absence of droplets, the flow field evolves to linearly forced HIT that is statistically stationary and in agreement with published results [42].

The droplets are randomly seeded in the flow and released from rest. The turbulent two-phase flow is forced for sufficient time such that the memory of the droplet initial conditions is lost as quantified by the droplets' Lagrangian integral time scale.

4. Results

In this section, we first present results for the single-droplet evaporation Cases 1–3 in which d_0/η is varied and proceed by discussing the multi-droplet Cases 4–6 in which α_l is varied. The single-droplet cases primarily serve as validation of the DNS flow solver. For the multi-droplet cases we seek to answer questions relating to the effect of inter-droplet spacing.

4.1. Effect of Reynolds number on evaporation rate

In this section, DNS results for single droplet evaporation are compared against measurements of n -heptane droplets evaporating in HIT at elevated temperature and pressure [29]. We consider

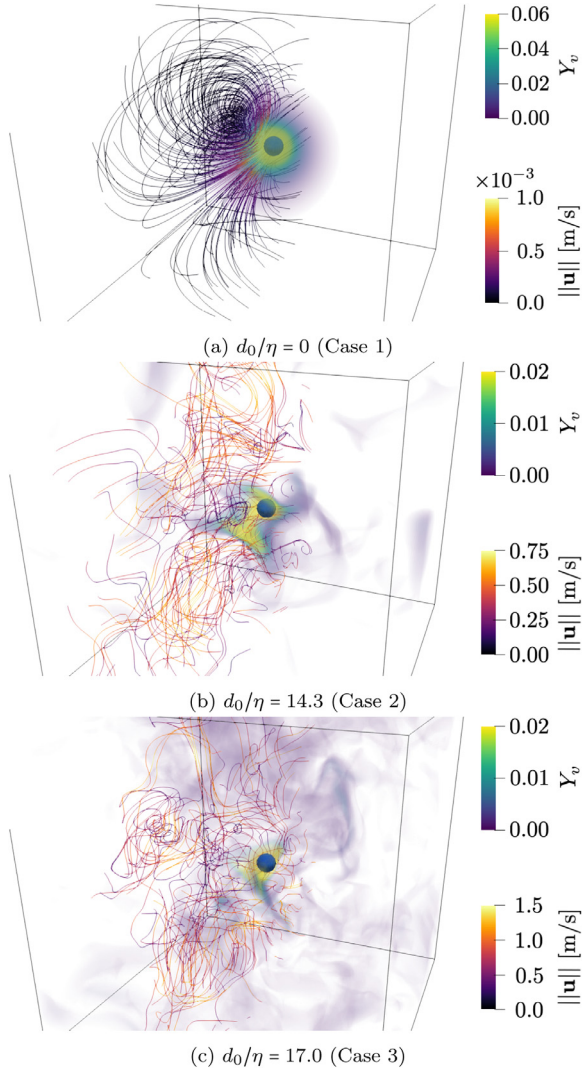


Fig. 1. Instantaneous streamlines at the final time ($t/d_0^2 = 1.68$ s/mm²) in half of the computational domain colored by velocity magnitude $\|\mathbf{u}\|$ and volume rendering of the vapor mass fraction Y_v field in the full domain for increasing d_0/η (Cases 1–3). The droplet interface is shown in blue ($C = 0.5$ isosurface). (For interpretation of the references to color in this figure legend, the reader is referred to the web version of this article.)

a quiescent case and two turbulent cases in which we set the turbulence forcing such that the turbulence intensity matches that of the experimental data corresponding to fan speeds of 500 and 1000 RPM (our Cases 2 and 3, respectively). Initially, the droplet is at rest and the gas phase is devoid of *n*-heptane vapor. The simulations are run for 75 ms, at which point the droplet evaporation rates have reached a statistically stationary state. Note that this corresponds to approximately 50 integral timescales for the highest turbulence intensity case.

Fig. 1 shows instantaneous snapshots from Cases 1–3 depicting streamlines and the vapor mass fraction field at $t/d_0^2 = 1.68$ s/mm². For the quiescent Case 1, the streamlines emanating from the droplet surface are caused by the Stefan flow due to the velocity jump at the liquid–gas interface from phase change. The vapor cloud remains spherically symmetric in the absence of any external flow or body force. In the turbulent Cases 2 and 3, the *n*-heptane vapor is transported away from the droplet surface and mixed by the surrounding turbulent eddies. As the Reynolds number increases, the extent to which the vapor fills the domain also

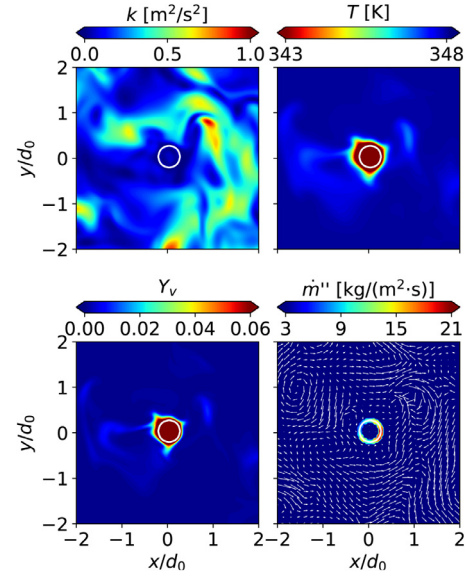


Fig. 2. Instantaneous contours for Case 3 at $t/d_0^2 = 1.68$ s/mm² of TKE k , temperature T , vapor mass fraction Y_v , and evaporative mass flux \dot{m}'' with velocity vectors projected in the $x - y$ plane. The white line shows the droplet interface. In the third panel, the interior of the droplet is pure *n*-heptane denoted by $Y_v = 1$.

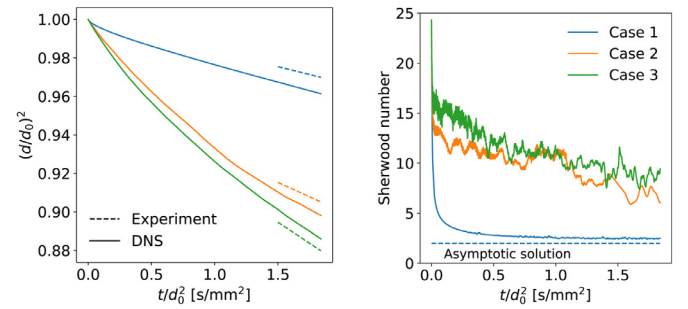


Fig. 3. Temporal evolution of the square of the normalized droplet diameter $(d/d_0)^2$ and Sherwood number Sh for varying d_0/η corresponding to Cases 1–3. The dashed lines are the steady-state evaporation rates from the experiments of [29].

increases. The droplets do not break up and remain nearly spherical because of their small Weber number $We_{rms} \ll 1$.

Fig. 2 shows instantaneous cross sections of turbulence kinetic energy k , T , Y_v , and \dot{m}'' , in a midplane of the domain at $t/d_0^2 = 1.68$ s/mm² for Case 3. The droplet enhances the local dissipation rate of TKE by enhancing the local velocity gradients near the droplet interface. Consequently, the TKE near the droplet surfaces is attenuated [43]. The structure of the temperature field and the vapor mass fraction field are self-similar owing to their similar transport equations. The vapor mass fraction field has more fine-scale structures than the temperature field as a consequence of the large Lewis number ($Le = 3.93$). The last panel in Fig. 2 shows that the evaporative mass flux \dot{m}'' on the droplet surface is highly non-uniform, a behavior not captured by point-particle methods. Regions of high \dot{m}'' are associated with large normal gradients in Y_v , corresponding to areas where the *n*-heptane vapor boundary layer is thinner.

To validate the DNS results, the square of the normalized droplet diameter $(d/d_0)^2$ is computed in time and compared against the steady-state values of the experiment. Fig. 3 shows the development of $(d/d_0)^2$ and the Sherwood number Sh for Cases 1–3. After an initial transient period, the DNS results closely match the experimentally measured evaporation rates, and Case 1 reaches the asymptotic solution for single droplets evaporating in a qui-

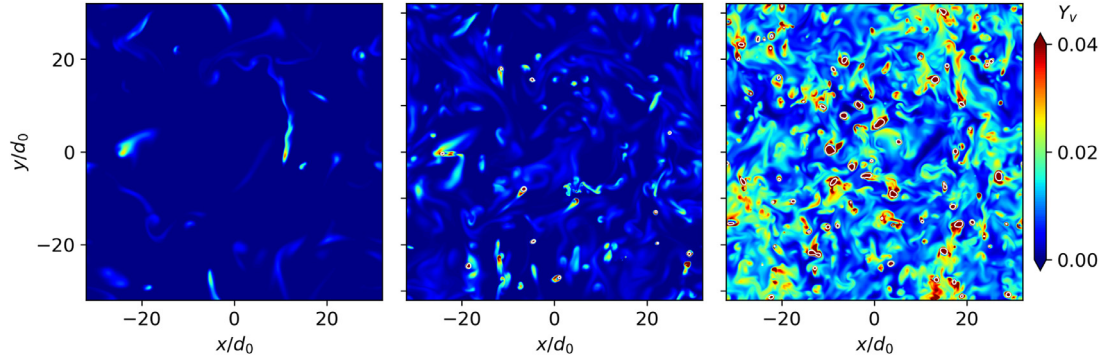


Fig. 4. Instantaneous contours at $t/d_0^2 = 0.5$ s/mm² of vapor mass fraction Y_v for varying liquid volume fraction α_l . From left to right, $\alpha_l = 10^{-4}$ (Case 4), $\alpha_l = 10^{-3}$ (Case 5), and $\alpha_l = 10^{-2}$ (Case 6). The white lines denote the droplet interfaces. The interior of the droplets are pure *n*-heptane denoted by $Y_v = 1$.

Table 2

Comparison of steady-state evaporation rates K from the experiment and DNS for Cases 1–3. The rightmost column shows the relative percentage difference ($100 \times (K_{\text{DNS}} - K_{\text{exp}})/K_{\text{exp}}$).

Case	K_{exp} (mm ² /s)	K_{DNS} (mm ² /s)	% difference
1	0.0164	0.0174	6.0
2	0.0298	0.0326	9.5
3	0.0436	0.0473	8.6

Table 3

Number of droplets N_d at the time of droplet introduction ($t = 0$), at the final time ($t = t_{\text{final}}$), and the corresponding percentage change.

Case	$N_d(t = 0)$	$N_d(t = t_{\text{final}})$	% change
4	51	53	3.9
5	501	545	8.8
6	5007	2883	−42.4

escent environment of $Sh = 2$. To better quantify the agreement, we compute the DNS evaporation rate K_{DNS} as $d^2 = d_0^2 - K_{\text{DNS}}t$ by time-averaging the evaporation rate over the last 3.2 ms of the simulation. The comparison of the experimental and DNS evaporation rates are reported in Table 2. Considering the uncertainties in reproducing the turbulence inside the experimental chamber and replicating the effects of the droplet suspension device, good agreement is achieved as indicated by a relative error of less than 10% for all cases.

4.2. Effect of liquid volume fraction on evaporation rate

We now explore the effect of increasing liquid volume fraction α_l on the evaporation rate. We increase α_l by increasing the number of droplets N_d such that the inter-droplet spacing decreases. For sufficiently high liquid volume fraction, it is expected that droplet-droplet interactions become important [43]. In the context of particle-laden flows this corresponds to the so-called “four-way” coupling regime [44]. These effects are also present for evaporating droplets, but with the additional complexity of the thermal and vapor fields of the neighboring droplets interacting with one another.

Two-dimensional contours of the vapor mass fraction field Y_v in an arbitrary $x - y$ plane are shown in Fig. 4. While for $\alpha_l = 10^{-4}$ the droplets remain relatively isolated, it is clear that for $\alpha_l = 10^{-2}$ the droplet-droplet interactions become important for two reasons: (i) droplet-droplet collisions occur which can lead to coalescence of two or more droplets and (ii) the droplet hydrodynamic, thermal, and vapor wakes impact nearby droplets.

4.2.1. Droplet bulk properties

In Fig. 5 the square of the normalized equivalent droplet diameter $(V_l/V_{l,0})^{2/3}$, total normalized droplet surface area A/A_0 , and Sauter mean diameter

$$\bar{d}_{32} = \frac{6V_l}{A} \quad (7)$$

are shown. The overbar notation $\bar{\cdot}$ is used to denote quantities that are system representative, i.e. a function of bulk and average values. As α_l increases the rate of decay of V_l decreases. In all

cases, the equivalent spherical diameter follows the “ d^2 -law” initially with $K \approx 0.085$ mm²/s. For later times, the case with highest α_l (Case 6) deviates from the d^2 -law behavior due to droplet-droplet interactions. In agreement with the existing literature, this implies that point-particle evaporation models based on the evaporation of isolated droplets are not appropriate for flows with high liquid volume fraction ($\alpha_l > 10^{-3}$) in which droplet-droplet interactions become important. Areas of relevance would be near an injector and regions of preferential concentration of droplets induced by turbulence.

The total droplet surface area initially decreases for all cases due to evaporation, but eventually starts to increase for Cases 4 and 5 ($\alpha_l = 10^{-4}$ and 10^{-3}) which is caused by aerodynamic forces exerted on the droplet surface leading to their deformation. Despite $We_{\text{rms}} \ll 1$ (Table 1), in HIT the instantaneous velocity can locally be significantly greater than the r.m.s. value [45], therefore for Cases 4–6 a subset of droplets will have Weber numbers $We_{\text{rms}} > 1$, leading to deformation and the observed increase in surface area. The monotonic decrease in surface area for Case 6 with $\alpha_l = 10^{-2}$ is explained by droplet evaporation at early times and droplet merging at later times due to significant droplet-droplet interaction at the high value of α_l .

To quantify the amount of breakup and coalescence, we counted the number of droplets at the start and end of the simulation. Our droplet identification algorithm first clips cells that contain VoF less than 0.5 in order to only identify those droplets that have sufficient mass and reduce “bridging” effects of two nearby droplets. After this, the flood fill algorithm is used to uniquely tag individual droplets. The results are shown in Table 3. Cases 4 and 5 show a slight increase (+3.9% and +8.8%, respectively) in the number of droplets between $t = 0$ and t_{final} due to droplet breakup and Case 6 shows a significant (−42%) decrease in the number of droplets due to coalescence. These results help explain the observations made in Fig. 5.

To quantify the convective heat and mass transfer from the droplet, we compute system-representative droplet Nusselt and Sherwood numbers

$$\overline{Nu} = \frac{\bar{h}_{\text{temp}} \bar{d}_{32}}{\bar{\lambda}_{\Sigma}} \quad \text{and} \quad \overline{Sh} = \frac{\bar{h}_{\text{mass}} \bar{d}_{32}}{\bar{\mathcal{D}}_{\Sigma}}, \quad (8)$$

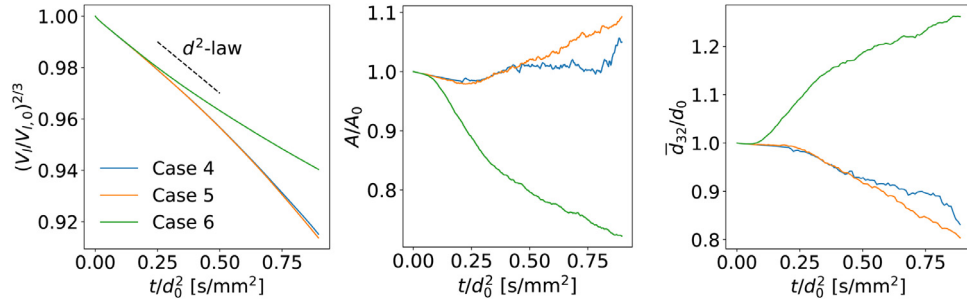


Fig. 5. Temporal evolution of the square of the normalized equivalent droplet diameter $(V/V_0)^{2/3}$, the normalized total droplet surface area A/A_0 , and the normalized Sauter mean diameter \bar{d}_{32}/d_0 .

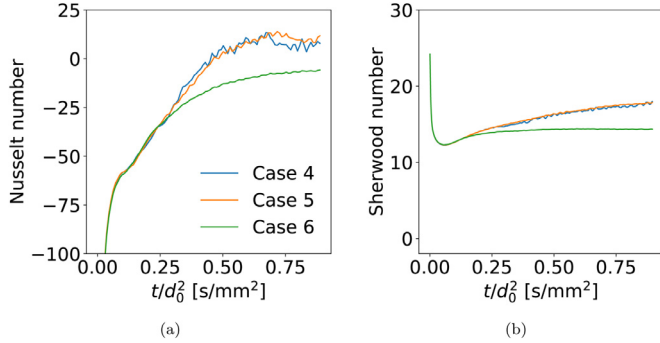


Fig. 6. Temporal evolution of the Nusselt number and Sherwood number for Cases 4–6.

where $\bar{\lambda}_\Sigma = \lambda(\langle T \rangle_\Sigma)$ and $\bar{\mathcal{D}}_\Sigma = \mathcal{D}(\langle T \rangle_\Sigma)$ are the mean thermal conductivity and mass diffusivity at the droplet surface. The brackets $\langle \cdot \rangle_\Sigma$ denote ensemble averaging of the enclosed quantity over all computational cells containing the interface. The quantities \bar{h}_{temp} and \bar{h}_{mass} are the system representative heat and mass transfer coefficients calculated as

$$\bar{h}_{\text{temp}} = \frac{\dot{Q}}{A (\langle T \rangle_\Sigma - T_\infty)} \quad \text{and} \quad \bar{h}_{\text{mass}} = \frac{\dot{M}}{A \rho_g (\langle Y_v \rangle_\Sigma - Y_{v,\infty})}, \quad (9)$$

where \dot{Q} and \dot{M} are the instantaneous rate of change of the total droplet enthalpy and mass, respectively, T_∞ and $Y_{v,\infty}$ are the far-field temperature and vapor mass fraction, respectively, which are taken to be the initial values of the gas phase, and A is the total droplet surface area as in Fig. 5. Fig. 6 shows the time evolution of \bar{Nu} and \bar{Sh} . We adopt the sign convention that $\bar{Nu} > 0$ when, in the mean, droplets are being heated and $\bar{Sh} > 0$ when droplets are losing mass due to evaporation. The Nusselt number is initially negative due to convective cooling of the droplet by the combined effects of Stefan flow and turbulence. The effect of increasing the volume fraction is to increase the magnitude of the Nusselt number. The case with the highest mass loading (Case 6) has sufficient thermal inertia in the dispersed phase to continuously extract heat from the carrier phase through phase change, and thus \bar{Nu} remains negative during the times considered. In Cases 4 and 5, the droplets initially cool rapidly ($\bar{Nu} < 0$) during the development of the concentration/thermal boundary layer, but at later times the carrier-phase turbulence re-heats ($\bar{Nu} > 0$) the droplets. The change in sign of \bar{Nu} is due to the droplets and carrier phase being initially at the same temperature. If the droplets were injected into an environment where $T_g \gg T_l$, it would be expected that $\bar{Nu} > 0$ during the entirety of the evaporation process. With relevance to combustion, this competition between heat-exchange processes was found to affect fuel spray ignition [19].

The Sherwood number is initially equal in all cases but, at later times, decreases for increasing α_l . At later times, Sh is nearly constant in time, indicating that quasi-steady evaporation is achieved, which corresponds to behavior similar to that predicted by the d^2 -law. The convective mass transfer due to turbulence leads to a Sherwood number that is significantly larger than the value of $Sh = 2$ found in quiescent droplet evaporation.

4.2.2. Droplet surface statistics

To further quantify the effect of α_l on the evaporation characteristics of the droplets, we compute the mean and r.m.s. values of the evaporative mass flux \dot{m}'' and the vapor mass fraction Y_v at the droplet surface as well as the mean droplet surface temperature $\langle T \rangle_\Sigma$. Fig. 7 shows that as α_l increases, $\langle \dot{m}'' \rangle_\Sigma$ and $\langle Y_v \rangle_\Sigma$ decrease. Recall that for Cases 4 and 5, Fig. 5 shows that the total surface area of the droplets increases in time and Fig. 7 shows that the mass flux also increases in time. Both effects contribute to steepening the evaporation curve compared to the initial d^2 -law behavior, shown in Fig. 5. In contrast, Case 6 shows slower evaporation due to reduced mass flux \dot{m}'' (Fig. 7) and surface area (Fig. 5) as a consequence of droplet coalescence.

Also shown in Fig. 7 is that both $\langle (\dot{m}'')^2 \rangle_\Sigma^{1/2}$ and $\langle Y_v^2 \rangle_\Sigma^{1/2}$ increase with increasing α_l . An increase in the r.m.s. of the vapor mass fraction with increasing α_l has also been shown in DNS of point-droplets in HIT [46]. In the present droplet-resolved simulations, we are able to capture the increase in vapor mass fraction variance directly on the droplet surface. The mean droplet surface temperature $\langle T \rangle_\Sigma$ is perfectly correlated with $\langle Y_v \rangle_\Sigma$ as expected through the use of the Antoine equation [30] for the computation of the surface vapor pressure. Since gas and liquid phases are initially at equal temperatures, a reduction in surface temperature is expected due to heat losses during phase change driven by surface vapor concentration gradients. This was illustrated for the case of a single evaporating droplet in Fig. 2.

To characterize the effect of droplet surface topology on the evaporation rate and its sensitivity to α_l , the final panel of Fig. 7 shows the normalized mean droplet curvature as a function of time $\langle \kappa \rangle_\Sigma / \kappa_0$, where $\kappa_0 = 0.1 \mu\text{m}^{-1}$, the initial curvature of the droplets, is equivalent for Cases 4–6. It shows that $\langle \kappa \rangle_\Sigma$ is non-monotonic with increasing α_l . The case with highest α_l (Case 6) has the lowest $\langle \kappa \rangle_\Sigma$, which is explained by droplet coalescence that was shown in Table 3 since larger droplets have smaller curvature. The case with highest $\langle \kappa \rangle_\Sigma$ (Case 5) has the greatest rate of droplet breakup as shown in Table 3. Comparing the first and last panel in Fig. 7 shows that cases with higher $\langle \kappa \rangle_\Sigma$ have higher $\langle \dot{m}'' \rangle_\Sigma$. The results suggest that surface deformation and breakup, leading to higher surface curvature, is associated with higher evaporation rates.

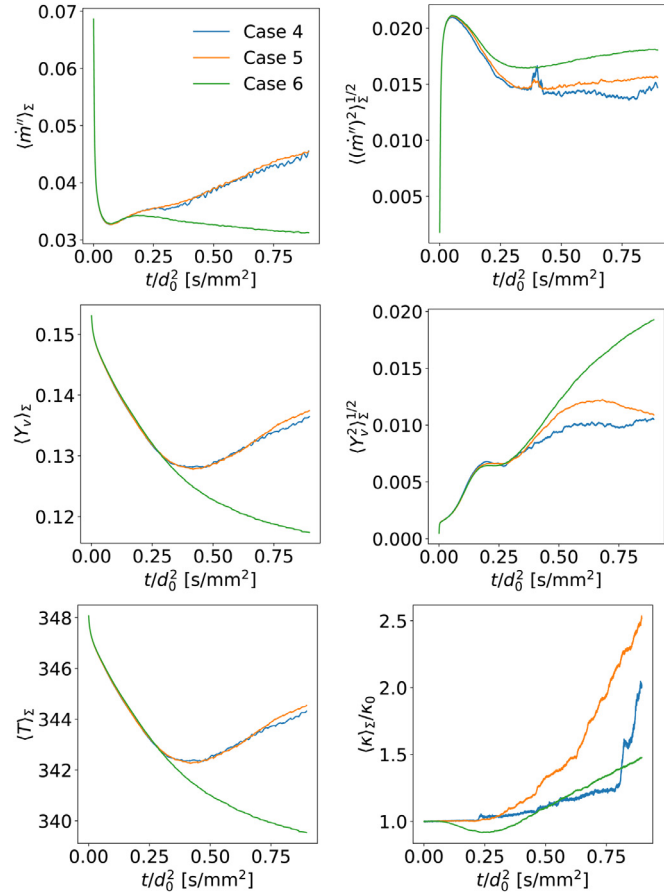


Fig. 7. Temporal evolution of the mean and r.m.s. of the evaporation rate \dot{m}'' , the mean and r.m.s. of the vapor mass fraction at the droplet surface $Y_{v,\Sigma}$, the mean droplet surface temperature $(T)_\Sigma$, and the normalized mean droplet surface curvature $(\kappa)_\Sigma/\kappa_0$ for Cases 4–6.

4.3. A priori analysis

In this section, the results of the DNS study will be considered in the context of models based on the point-particle approximation. Both single-droplet and multi-droplet cases will be considered. Limitations of the approximation and its associated models will be demonstrated, and the physical basis for those limitations will be discussed by applying them to the temporally-evolving DNS data in an *a priori* study.

From [8], in the point particle approximation the evaporation rate of a droplet can be expressed as

$$\frac{dm_d}{dt} = \frac{Sh}{3Sc_g} \left(\frac{m_d}{\tau_d} \right) \mathcal{H}_M, \quad (10)$$

where m_d is the droplet mass, Sc_g is the gas-phase Schmidt number, τ_d is the droplet relaxation time, now based on the instantaneous droplet diameter d , and \mathcal{H}_M is the mass transfer potential. In Eq. 10, both Sh and \mathcal{H}_M require modeling. For the former quantity, correlations of the type proposed by Frössling [47] and Ranz and Marshall [48] are in common use for point-particle simulations. For the latter, the classical rapid mixing model [49,50] is commonly employed, although more advanced models are also in use [8].

We consider first the temporal evolution of the Sherwood number. In the point-particle approximation, the spatial inhomogeneities in the rate of evaporation on the droplet surface due to its interaction with the turbulence cascade and its associated range of scalar and momentum scales cannot be evaluated, and

must thus be captured by the Sherwood number model employed. We compare such an approach quantitatively to the single droplet Cases 1–3 by evaluating Sh *a priori* using two single-droplet mass-transfer correlations from the literature and comparing it to the Sherwood number computed directly from the DNS as per Eqs. (8) and (9). The first is the well-known Frössling correlation for forced convective flow over a sphere [47]

$$Sh = 2 + 0.552Re_d^{1/2}Sc_g^{1/3}, \quad (11)$$

where $Re_d = \rho_g U_\infty d / \mu_g$ is the droplet Reynolds number based on the free-stream convective velocity U_∞ . In the present case of a droplet in HIT, where there is no mean convective velocity, we will take $U_\infty = U_{rms}$, which is temporally constant in the present forced HIT. The second correlation is that due to Birouk and Gökalt for a droplet in turbulent flow with zero mean velocity [51]

$$Sh = 2 + 0.04Re_{t,d}^{2/3}Sc_g^2, \quad (12)$$

where $Re_{t,d} = \rho_g U_{rms} d / \mu_g$ is the turbulence droplet Reynolds number.

Eqs. (11) and (12) can now be evaluated *a priori* at each time step from the instantaneous DNS data for ρ_g , μ_g and d , with physical properties evaluated using the 1/3-rule [8] between their gas-phase instantaneous surface-averaged and domain-averaged values. The DNS data and point-particle data evaluated *a priori* using the two models considered for the temporal evolution of Sh are plotted in Fig. 8a for Cases 1–3. We see that for Case 1 ($Re_d = 0$) the DNS results asymptotically approach the value of $Sh = 2$ as expected from Eqs. (11) and (12). For Cases 2 and 3, the DNS data approaches the Sherwood number computed from Eq. (11) while the Sherwood number computed from Eq. (12) is approximately 50% less than the DNS results.

Fig. 8b compares the Sherwood number for Cases 4–6 from the DNS to that computed *a priori* using the models Eqs. (11) and (12). The results show that the models underpredict the Sherwood number in all cases by approximately a factor of three to five, with Eq. (11) demonstrating better agreement than Eq. (12). The models also predict Case 6 to have the highest Sh in contrast to the DNS results. This is due to Re_d increasing in time as a consequence of \bar{d}_{32} increasing as shown in Fig. 5. Because d/η is much smaller in Cases 4–6 than Cases 2 and 3, the Frössling correlation is closer to the d/η parameter range for which it was developed in Cases 4–6. However, the performance of both correlations (Eqs. (11) and (12)) is expected to deteriorate due to multi-droplet effects.

We consider next the droplet vaporization rate dm_d/dt in Cases 4–6. In the context of multi-droplet evaporation simulations employing the point-particle approximation, in addition to being unable to directly capture surface inhomogeneities for individual droplets, the effects of droplet-droplet interactions require further modeling. Furthermore, the inhomogeneity of vapor mass fraction throughout the domain requires the spatial resolution of the scales of scalar motion on the order of the droplet size. This causes issues with the common numerical methods employed, since the liquid volume fraction in any given computational cell may then approach unity, and the interaction of the droplet with the gas phase can no longer be reasonably represented as a point source. Another approach is to coarse-grain the effect of the spatial inhomogeneities by assuming rapid scalar mixing due to turbulence on the scale of multiple droplets. The approach in the present *a priori* study amounts to treating the domain as a single Eulerian cell. This is an extreme case of coarse-graining, and is not intended to be a quantitative representation of modern point-particle methods. Rather, it provides a qualitative illustration of the effect of the loss of information that occurs in the point-particle approximation in a limiting case.

The rate of evaporation of a single point-particle is described by the right-hand-side of Eq. (10). Instead of computing dm_d/dt for

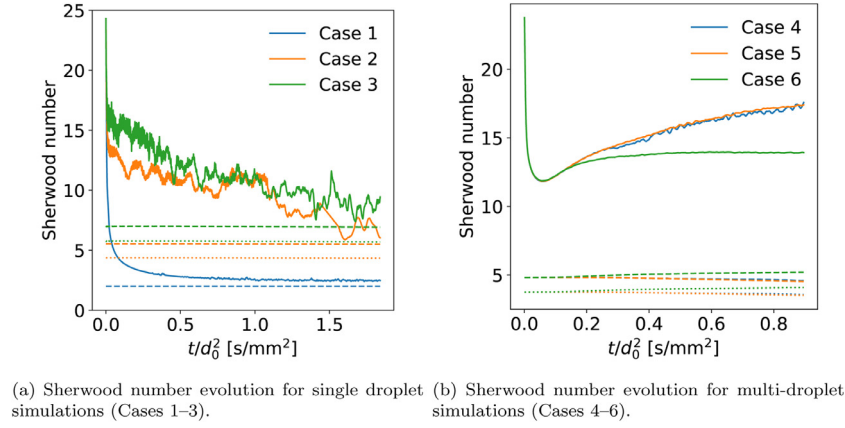


Fig. 8. A priori analysis of DNS data using models based on the point particle approximation. DNS: — Eq. (11); - - -, Eq. (12); · · · .

individual droplets and averaging, we compute the rate of change of the mass of the dispersed phase $\dot{M} = dM/dt$, by computing Sh , M , and τ_d from the DNS data using their associated definitions and the quantities ρ_g , μ_g , and d from the instantaneous DNS data. Physical quantities are evaluated as in the single-droplet study, but using surface properties of the mean droplet, and the droplet diameter is taken as the Sauter mean diameter, which accounts for droplet deformation. The mass transfer potential \bar{H}_M is evaluated using the rapid mixing model [49,50] $\bar{H}_M = \ln(1 + \bar{B}_M)$, where \bar{B}_M is the system-representative Spalding number for mass transfer, evaluated as

$$\bar{B}_M = \frac{\langle Y_v \rangle_\Sigma - \langle Y_v \rangle_g}{1 - \langle Y_v \rangle_\Sigma}, \quad (13)$$

where $\langle \cdot \rangle_g$ denotes spatial averaging of the enclosed quantity over the gas phase. From the DNS data, we compute the rate of change of the total droplet mass directly as

$$\frac{dM}{dt} = \rho_l \frac{d}{dt} \int_V dV. \quad (14)$$

The DNS data and point-particle data evaluated a priori for the temporal evolution of $\dot{M} = dM/dt$ normalized by the evaporation rate in stagnant ($Re_d = 0$) conditions \dot{M}_s are plotted in Fig. 9a for Cases 4–6, where Eq. (11) was used to compute Sh for the point-particle data. We see that the point-particle model evaluated a priori underpredicts the evaporation rate by about a factor of three in all cases.

To understand this, we analyze the relative magnitudes of the terms in Eq. (10), which are shown in Figs. 8b and 9. The total droplet mass M and relaxation time based on the Sauter mean diameter $\bar{\tau}_d$ are computed directly via DNS data. Therefore, they should be treated as exact in an a priori sense. They are still presented for completeness. As previously observed in Fig. 8b, the model underpredicts the Sh by a factor of approximately three, which leads to the disagreement observed in Fig. 9a. Finally, Fig. 9d shows that the system representative mass transfer potential \bar{H}_M decreases significantly with increasing volume fraction α_l . This behavior correctly modulates the evaporation rate \dot{M} with respect to α_l , such that if the Sh model were improved, the agreement between the DNS and model for \dot{M} would be satisfactory. The correct \bar{H}_M behavior shows that, in turbulent homogeneous flows, it is justifiable to compute $\langle Y_v \rangle_g$ in Eq. (13) by assuming that vapor is rapidly mixed upon evaporation to account for multi-droplet/group evaporation effects. Non-homogeneous flows and droplet distributions could use a similar approach but with a more refined model for $\langle Y_v \rangle_g$ [4,52–54].

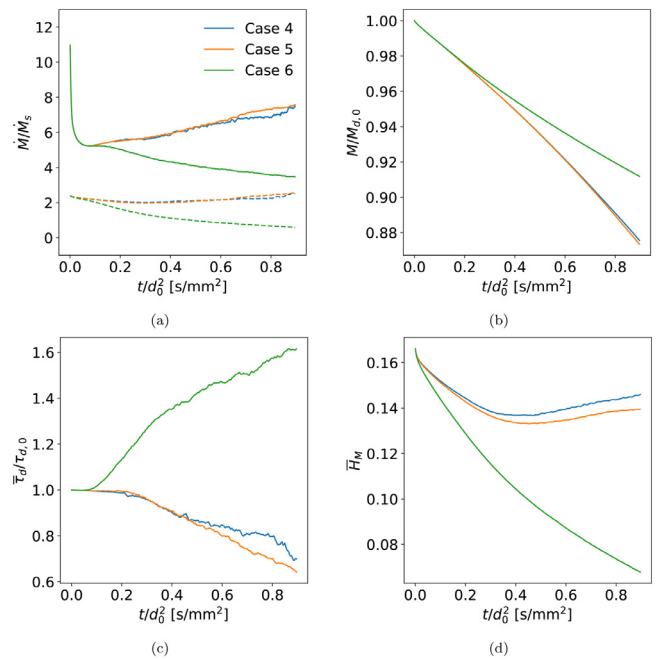


Fig. 9. The time evolution of the droplets' evaporation rate \dot{M} normalized by the evaporation rate in stagnant conditions \dot{M}_s , normalized total droplet mass M/M_0 , normalized droplet relaxation time $\bar{\tau}_d/\tau_{d,0}$, and system-representative mass transfer potential \bar{H}_M for Cases 4–6. DNS: — Eq. (10); - - -, Eq. (11).

5. Conclusions

A parametric study was performed to analyze the effects of d_0/η and α_l on the evaporation rate of *n*-heptane droplets in homogeneous isotropic turbulence at elevated temperatures and pressures via DNS. The DNS results for the evaporation rate of a droplet in HIT were compared with the experimental results of an *n*-heptane droplet evaporating in HIT [29]. The calculated evaporation rates from the DNS were within 10% of the experimentally measured values. Increasing the liquid volume fraction led to a decrease in the evaporation rate due to a decrease in the mass transfer potential. The DNS results show that at high liquid volume fraction ($\alpha_l = 10^{-2}$) the droplets evaporate more slowly than what would be predicted from the classical d^2 -law. This was shown to be primarily caused by a decrease in the mass transfer potential and secondarily by a reduction in the droplet surface area due to droplet-droplet merging.

The DNS-data were utilized in an *a priori* study to examine the accuracy of commonly employed point-particle models. Results from this study showed the importance of accurately predicting the Sherwood number in turbulent flow conditions. Both the Frössling and Birouk-Gökulp correlations were analyzed and shown to underpredict droplet evaporation rates. This study has thus provided insight regarding the limitations of point-particle methods and the causes thereof, and the results can be used in advancing the models adopted in point-particle methods.

Declaration of Competing Interest

The authors declare that they have no known competing financial interests or personal relationships that could have appeared to influence the work reported in this paper.

CRediT authorship contribution statement

Michael S. Dodd: Conceptualization, Formal analysis, Investigation, Methodology, Software, Writing - original draft. **Danyal Mohaddes:** Conceptualization, Formal analysis, Investigation, Writing - original draft. **Antonino Ferrante:** Supervision, Writing - review & editing. **Matthias Ihme:** Conceptualization, Funding acquisition, Resources, Supervision, Writing - review & editing.

Acknowledgments

The authors thank Mr. Cameron Verwey and Prof. Madjid Birouk for providing the experimental droplet evaporation rates. Financial support from NASA Award no. NNX15AV04A and ONR Grant no. 9371 is gratefully acknowledged. Computational resources supporting this work were provided by the NASA High-End Computing (HEC) Program through the NASA Advanced Supercomputing (NAS) Division at Ames Research Center and the National Energy Research Scientific Computing Center (NERSC), a U.S. Department of Energy Office of Science User Facility operated under Contract no. DE-AC02-05CH11231. A. F. is grateful to Prof. Parviz Moin and the Center for Turbulence Research for the support provided for his sabbatical of Winter 2019 at Stanford University.

Appendix A. Convergence of the DNS results with grid size

In this section we discuss numerical resolution of the smallest length scales of the flow and present the convergence of the DNS results for Case 3 on 224^3 and 448^3 grids. This case is chosen because it has the highest Reynolds number of the single droplet cases (Cases 1–3). The smallest length scales for mixing of passive scalars in HIT are the Kolmogorov scale η and the Batchelor scale [55]

$$\lambda_B = \frac{\eta}{\sqrt{Sc}}. \quad (\text{A.1})$$

The commonly accepted DNS resolution criteria [45,56,57] are $\kappa_{\max}\eta \geq 1.5$ and, analogously, $\kappa_{\max}\lambda_B \geq 1.5$, where κ_{\max} is the maximum resolved wavenumber ($\kappa_{\max} = \pi N/L$). Table A.4 shows $\kappa_{\max}\eta$ and $\kappa_{\max}\lambda_B$ for the turbulent Cases 2–6. This table shows that in all cases the numerical resolution criteria are satisfied. Notably, for the multi-droplet DNS Cases 4–6, the requirements are exceeded by at least a factor of four.

To quantify the convergence of the DNS results, we computed the L_1 convergence between quantities of interest on the 224^3 and 448^3 grids as

$$E_\phi = \frac{1}{N} \sum_{i=1}^N \left| \frac{\phi_{i,448} - \phi_{i,224}}{\phi_{i,448}} \right| \quad (\text{A.2})$$

Table A1

Numerical resolution of the Kolmogorov η and Batchelor λ_B scales for turbulent flow DNS Cases 2–6, where κ_{\max} is the maximum resolved wavenumber ($\kappa_{\max} = \pi N/L$).

Case	$\kappa_{\max}\eta$	$\kappa_{\max}\lambda_B$
2	3.08	1.84
3	2.59	1.54
4	10.9	6.51
5	10.9	6.51
6	10.9	6.51

Table A2

Grid convergence study for Case 3 on 224^3 and 448^3 grids. The relative L_1 convergence given by Eq. (A.2) is shown for the mean droplet temperature ($\langle T_d \rangle$), droplet volume (V_d), mean vapor mass fraction at the droplet surface ($\langle T \rangle_\Sigma$), and the mean evaporative mass flux at the droplet surface ($\langle \dot{m}'' \rangle_\Sigma$).

ϕ	E_ϕ
$\langle T_d \rangle$	0.004 %
V_d	0.09 %
$\langle T \rangle_\Sigma$	0.9 %
$\langle \dot{m}'' \rangle_\Sigma$	14.0 %

for N equally spaced observations in the interval $t/d_0^2 = [0.0096, 0.0120]$ s/mm². We note that the numerical accuracy of evaporating droplet simulations decreases with time, since the number of grid points resolving each droplet decreases. However, in the simulations considered in the paper, this decrease amounts to approximately 5% over the time interval considered, and a corresponding maximum resolution reduction of approximately half a grid point when droplets are initially resolved using 14 points per diameter.

Table A.5 shows the L_1 convergence E_ϕ for the mean droplet temperature, droplet volume, mean vapor mass fraction at the droplet surface, and mean evaporative mass flux. The table shows that the DNS results ($\langle T_d \rangle$, V_d , $\langle T \rangle_\Sigma$) are practically unchanged when the grid resolution is increased from 224^3 to 448^3 . The mean evaporative mass flux ($\langle \dot{m}'' \rangle_\Sigma$) shows larger sensitivity to the grid. We hypothesize that this is related to $Sc_g > 1$ and because $\langle \dot{m}'' \rangle_\Sigma$ is a function of the interfacial gradient of Y_ν via Eq. (4), and therefore the scalar field convergence is slower than momentum and energy. This indicates that the smallest lengthscale of the flow is associated with the Y_ν boundary layer at the liquid-gas interface. This is consistent with findings in non-evaporating flows [58] showing the smallest hydrodynamic lengthscale is located at the droplet interface.

References

- [1] M. Birouk, I. Gökalp, Current status of droplet evaporation in turbulent flows, *Prog. Energy Combust. Sci.* 32 (4) (2006) 408–423.
- [2] P. Jenny, D. Roekaerts, N. Beishuizen, Modeling of turbulent dilute spray combustion, *Prog. Energy Combust. Sci.* 38 (6) (2012) 846–887.
- [3] A. Lefebvre, A. Arrowsmith, *Atomization and Sprays*, CRC Press, 2017.
- [4] W.A. Sirignano, *Fluid Dynamics and Transport of Droplets and Sprays*, Cambridge University Press, 2010.
- [5] S. Dhanuka, J.F. Driscoll, H. Mongia, Instantaneous flow structures in a reacting gas turbine combustor, *AIAA Paper* 2008-4683 (2008).
- [6] Q. Wang, T. Jaravel, M. Ihme, Assessment of spray combustion models in large-eddy simulations of a polydispersed acetone spray flame, *Proc. Combust. Inst.* 37 (3) (2019) 3335–3344.
- [7] J.G.M. Kuerten, Point-particle DNS and LES of particle-laden turbulent flow—a state-of-the-art review, *Flow Turbul. Combust.* 97 (3) (2016) 689–713.
- [8] R.S. Miller, K. Harstad, J. Bellan, Evaluation of equilibrium and non-equilibrium evaporation models for many-droplet gas-liquid flow simulations, *Int. J. Multiph. Flow* 24 (1998) 1025–1055.
- [9] R.O. Fox, A. Varma, *Computational Models for Turbulent Reacting Flows*, Cambridge University Press, 2003.
- [10] A. Vié, F. Laurent, M. Massot, Size-velocity correlations in hybrid high order moment/multi-fluid methods for polydisperse evaporating sprays: modeling and numerical issues, *J. Comput. Phys.* 237 (2013) 177–210.
- [11] F. Mashayek, Droplet-turbulence interactions in low-Mach-number homogeneous shear two-phase flows, *J. Fluid Mech.* 367 (1998) 163–203.

- [12] R.S. Miller, J. Bellan, Direct numerical simulation of a confined three-dimensional gas mixing layer with one evaporating hydrocarbon-droplet-laden stream, *J. Fluid Mech.* 384 (1999) 293–338.
- [13] J. Reveillon, F. Demoulin, Evaporating droplets in turbulent reacting flows, *Proc. Combust. Inst.* 31 (2) (2007) 2319–2326.
- [14] J. Xia, K. Luo, Direct numerical simulation study of evaporation effects in combustion suppression by inert droplets, *Proc. Combust. Inst.* 33 (2) (2011) 2581–2590.
- [15] M.R.G. Zoby, S. Navarro-Martinez, A. Kronenburg, A.J. Marquis, Evaporation rates of droplet arrays in turbulent reacting flows, *Proc. Combust. Inst.* 33 (2) (2011) 2117–2125.
- [16] K. Luo, H. Pitsch, M. Pai, O. Desjardins, Direct numerical simulations and analysis of three-dimensional *n*-heptane spray flames in a model swirl combustor, *Proc. Combust. Inst.* 33 (2011) 2143–2152.
- [17] A. Vié, B. Franzelli, Y. Gao, T. Lu, H. Wang, M. Ihme, Analysis of segregation and bifurcation in turbulent spray flames: a 3D counterflow configuration, *Proc. Combust. Inst.* 35 (2015) 1675–1683.
- [18] Q. Wang, X. Zhao, M. Ihme, A regularized deconvolution model for sub-grid dispersion in large eddy simulation of turbulent spray flames, *Combust. Flame* 207 (2019) 89–100.
- [19] P.B. Govindaraju, T. Jaravel, M. Ihme, Coupling of turbulence on the ignition of multicomponent sprays, *Proc. Combust. Inst.* 37 (2019) 3295–3302.
- [20] S. Elghobashi, Direct numerical simulation of turbulent flows laden with droplets or bubbles, *Annu. Rev. Fluid Mech.* 51 (2019) 217–244.
- [21] D. Juric, G. Tryggvason, Computations of boiling flows, *Int. J. Multiph. Flow* 24 (3) (1998) 387–410.
- [22] S.W.J. Welch, J. Wilson, A volume of fluid based method for fluid flows with phase change, *J. Comput. Phys.* 160 (2) (2000) 662–682.
- [23] S. Tanguy, T. Ménard, A. Berlemont, A level set method for vaporizing two-phase flows, *J. Comput. Phys.* 221 (2) (2007) 837–853.
- [24] J. Schlottke, B. Weigand, Direct numerical simulation of evaporating droplets, *J. Comput. Phys.* 227 (10) (2008) 5215–5237.
- [25] J. Shinjo, J. Xia, A. Umemura, Droplet/ligament modulation of local small-scale turbulence and scalar mixing in a dense fuel spray, *Proc. Combust. Inst.* 35 (2) (2015) 1595–1602.
- [26] J.A. Palmore, O. Desjardins, Direct numerical simulations of turbulent multi-phase flows undergoing evaporation, *AIAA Paper* 2017-1704 (2017).
- [27] B. Duret, G. Luret, J. Reveillon, T. Ménard, A. Berlemont, F.-X. Demoulin, DNS analysis of turbulent mixing in two-phase flows, *Int. J. Multiph. Flow* 40 (2012) 93–105.
- [28] G. Lupo, M.N. Ardekani, L. Brandt, C. Duwig, An immersed boundary method for flows with evaporating droplets, *Int. J. Heat Mass Transf.* 143 (2019) 118563.
- [29] C. Verwey, M. Birouk, Fuel vaporization: effect of droplet size and turbulence at elevated temperature and pressure, *Combust. Flame* 189 (2018) 33–45.
- [30] C. Antoine, Tensions des vapeurs; nouvelle relation entre les tensions et les températures, *C. R. Acad. Sci.* 107 (1888) 681–684.
- [31] W. Sutherland, LII. The viscosity of gases and molecular force, *Philos. Mag.* 36 (223) (1893) 507–531.
- [32] B.J. McBride, Coefficients for Calculating Thermodynamic and Transport Properties of Individual Species, 4513, NASA Langley Research Center, 1993.
- [33] D.G. Goodwin, R.L. Speth, H.K. Moffat, B.W. Weber, Cantera: an object-oriented software toolkit for chemical kinetics, thermodynamics, and transport processes, 2018. Version 2.4.0.
- [34] T. Lu, C.K. Law, C.S. Yoo, J.H. Chen, Dynamic stiffness removal for direct numerical simulations, *Combust. Flame* 156 (8) (2009) 1542–1551.
- [35] M.S. Dodd, Direct Numerical Simulation of Droplet-Laden Isotropic Turbulence, University of Washington, 2017 Ph.D. thesis.
- [36] M.S. Dodd, A. Ferrante, A fast pressure-correction method for incompressible two-fluid flows, *J. Comput. Phys.* 273 (2014) 416–434.
- [37] A. Baraldi, M.S. Dodd, A. Ferrante, A mass-conserving volume-of-fluid method: volume tracking and droplet surface-tension in incompressible isotropic turbulence, *Comput. Fluids* 96 (2014) 322–337.
- [38] J.U. Brackbill, D.B. Kothe, C. Zemach, A continuum method for modeling surface tension, *J. Comput. Phys.* 100 (2) (1992) 335–354.
- [39] A. Lefebvre, D. Ballal, *Gas Turbine Combustion*, CRC Press, 2010.
- [40] L. Esclapez, P.C. Ma, E. Mayhew, R. Xu, S. Stouffer, T. Lee, H. Wang, M. Ihme, Fuel effects on lean blow-out in a realistic gas turbine combustor, *Combust. Flame* 181 (2017) 82–99.
- [41] U. Schumann, Realizability of Reynolds-stress turbulence models, *Phys. Fluids* 20 (1977) 721.
- [42] C. Rosales, C. Meneveau, Linear forcing in numerical simulations of isotropic turbulence: physical space implementations and convergence properties, *Phys. Fluids* 17 (9) (2005) 095106.
- [43] M.S. Dodd, A. Ferrante, On the interaction of Taylor length scale size droplets and isotropic turbulence, *J. Fluid Mech.* 806 (2016) 356–412.
- [44] S. Elghobashi, On predicting particle-laden turbulent flows, *Appl. Sci. Res.* 52 (4) (1994) 309–329.
- [45] S.B. Pope, *Turbulent Flows*, Cambridge University Press, 2000.
- [46] P. Weiss, D.W. Meyer, P. Jenny, Evaporating droplets in turbulence studied with statistically stationary homogeneous direct numerical simulation, *Phys. Fluids* 30 (8) (2018) 083304.
- [47] N. Frössling, Über die Verdunstung fallender Tropfen, *Gerlands Beitr. Geophys.* 52 (1938) 170–216.
- [48] W.E. Ranz, W.R. Marshall, Evaporation from drops, Part I, *Chem. Eng. Prog.* 48 (3) (1952) 141–146.
- [49] G.A. Godsave, Studies of the combustion of drops in a fuel spray-the burning of single drops of fuel, *Symp. (Int.) Combust.* 4 (1953) 818–830.
- [50] D. Spalding, The combustion of liquid fuels, *Symp. (Int.) Combust.* 4 (1953) 847–864.
- [51] M. Birouk, I. Gökalp, A new correlation for turbulent mass transfer from liquid droplets, *Int. J. Heat Mass Transf.* 45 (1) (2002) 37–45.
- [52] H. Chiu, T. Liu, Group combustion of liquid droplets, *Combust. Sci. and Tech.* 17 (3–4) (1977) 127–142.
- [53] M. Labowsky, A formalism for calculating the evaporation rates of rapidly evaporating interacting particles, *Combust. Sci. and Tech.* 18 (3–4) (1978) 145–151.
- [54] R.T. Imaoka, W.A. Sirignano, Transient vaporization and burning in dense droplet arrays, *Int. J. Heat Mass Transf.* 48 (21–22) (2005) 4354–4366.
- [55] G.K. Batchelor, Small-scale variation of convected quantities like temperature in turbulent fluid part 1. General discussion and the case of small conductivity, *J. Fluid Mech.* 5 (1) (1959) 113–133.
- [56] M.R. Overholt, S.B. Pope, Direct numerical simulation of a passive scalar with imposed mean gradient in isotropic turbulence, *Phys. Fluids* 8 (11) (1996) 3128–3148.
- [57] J. Schumacher, K. Sreenivasan, P. Yeung, Very fine structures in scalar mixing, *J. Fluid Mech.* 531 (2005) 113–122.
- [58] M.S. Dodd, L. Jofre, Small-scale flow topologies in decaying isotropic turbulence laden with finite-size droplets, *Phys. Rev. Fluids* 4 (6) (2019) 064303.